Comparison of HMI Carrington Synotic Maps of Photospheric Magnetic Fields Between High and Low Spatial Resolutions

X. P. Zhao, J. T. Hoeksema, Y. Liu

Stanford University

— 2010 AGU Meeting of Americas—

August 08 – 13, 2010, Iguassu Falls, Brazil

1. Introduction

HMI, the Helioseismic and Magnetic Imager on SDO provides a synoptic series of full-disk arc-second magnetograms. The HMI Carrington synoptic map of line-of-sight photospheric magnetic field is constructed using 16366 12-minute HMI line-of-sight magnetograms collected over one solar rotation period, and merging onto a 3600 x 1440 synoptic grid of equal-area elements. Its spatial resolution is 0.1° heliographic. Such high spatial-resolution HMI Carrington synoptic map contains all magnetic features with length scale greater than 2.4 Mm, and can be used to study the relationship between small- and global-scale magnetic features.

The Carrington synoptic map is the basic input for various data-based coronal models. Many coronal structures are believed to be associated with the photospheric magnetic field of spatial scale much larger than 2.4 Mm.

This work tries to find out the spatial scales of magnetic features that are good for reconstruction of such large-scale coronal magnetic field and plasma structures as coronal holes, and

to determine the optimum principal index n used in various hydrostatic models, such as the PFSS and CSSS models.

2. HMI synoptic maps with various spatial resolutions

Using neiboring average, the HMI synoptic map with the grid of 3600x 1440 may be reduced to synoptic maps with grids of 720x360, 360x180, 180x90, 90x45, and 72x30, corresponding to lengh-scale of 12 Mm (0.5°), 24 Mm (1°), 48 Mm (2°), 96 Mm, (4°) and 120 Mm (6°). Figure 1 displays four HMI synoptic maps with the grids of 3600 x 1440, 360x180, 180x90, and 72x30, showing magnetic features with different length scales.

3. Spherical harmonics

With the assumption that there are no electric currents above the photospheric level of measurement, the global photospheric magnetic energy distribution can be analyzed in terms of contributions of different scale-size and geometric pattern. The spherical harmonic expansion provides essential information

needed to understand the pattern of the photospheric magnetic field and its evolution, and to monitor the quality of the data handing procedures.

Each spherical harmonic implicitly includes all functions of indices *n* and *m*, so that the numerical value of any coefficient g_n^m or h_n^m in the spherical harmonic expansion,

$$g_n^m = \frac{2n+1}{I\,J} \sum_{i=1}^{I} \sum_{j=1}^{J} B_r(\theta_i, \phi_j) P_n^m(\theta_i) \cos(m\phi_j) \qquad (1)$$

$$h_n^m = \frac{2n+1}{I\,J} \sum_{i=1}^{I} \sum_{j=1}^{J} B_{\rm ls}(\theta_i, \phi_j) P_n^m(\theta_i) \sin(m\phi_j) \qquad (2)$$

can be directly compared with that of any other coefficient regardless of *n* or *m*; The larger coefficient indicates an harmonic (*n*, *m*) contributing greater power to the expansion of the photospheric magnetic field. In Figure 2 we plot on a log scale the power spectrum P_n of the multipoles of the photospheric magnetic field. The multipolar spectrum is defined as

$$P_n = \sum_{m=0}^{n} [(g_n^m)^2 + (h_n^m)^2]/8\pi \qquad (3)$$

The red curve denotes the spectrum from the synoptic map of 3600x1440 and black curves from other maps with lower spatial resolution.. The vertical lines denote the values of principal index, n, that details of magnetic features smaller than about 1/(2n) of the solar circumference (or 360°/(2n)) could not be

discerned. For instance, for $n = 90$ in the top panel of right coloum of Figure 2, details of magnetic features smaller than 48 Mm (2°), which is just the spatial resolution of the 180x90 grid, could not be discerned.

The three panels in left coloum of Figure 2 show that the black curves are basically the same as red curve. It is understandable because all the three maps contain nearly the same magnetic features for length scale greater than 2°. For the right coloumn, the spectrums between black and red are basically the same when principal index n lower than the values corresponding to the vertical lines. The red curves become flat when n greater than 60. This change in the power spectrum around $n = 60$ may be associated with the distribution of proper motion velocities [Altschuler et al., 1977].

4. The effect of spatial resolution of synoptic maps on calculated foot-point of open field lines

In order to find out the optimum principal index for reconstructing coronal holes, the foot-points of open field lines, we first use the PFSS model, principal index of $n = 90, 70, 50, 30$,

and the harmonic coefficients obtained from HMI synopotic maps with various space grids. It is expected that the location of the foot-points depends on spatial resolution of maps as well as the principal index selected in the calculation. Figures 3a, 3b, and 3c show the effect, where red (blue) foot points denoting negative (positive) polarity are plotted over the corresponding HMI synoptic maps. Figure 3a shows that the predicted foot-points areas in the top three panels are basically identical, but the foot-point areas in the bottom panel is different from the others. panel

By comparing the predicted open-line foot-points with observed coronal holes we might be able to find out the optmum n. Figure 4 displays coronal holes observed at 2010.05.28_23:46:08 and 2010.06.05_23:15:56 by SDO/AIA. The two times correspond to 241.5° and 135.5°, i.e., the red and blue foot-point areas, respectively, in the middle of Figures 3.

Figures 5a and 5b compare the effect of map's spatial resolution on calculated open-field foot-point areas when $n = 90$ and $n = 30$. Figures 6a and 6b compare the effect of principal index n on the calculate d open-field foot-point areas when map's spatial resolution is fixed.

5. Summary and Discussions

5.1 The HMI Carrington synoptic map of the line-of-sight photospheric magnetic field with unprecedented high spatial resolution and low random noise provides an opotunity to more accurately calculate spherical hamonic coefficients and calculate the multipolar power spectrum distribution.

5.2 By comparing multipolar power spectrums obtained from synoptic maps with space grids of 3600x1440, 720x360, 360x180, 180x90, 90x45, and 72x30, we find that for space grids greater than 180x90 (spatial resolution higher than 2°) the multipolar power spectrum upto $n = 90$ are basically the same. However, there are significant artificial effect in the multipolar power spectrum upto $n = 90$ obtained from synoptic maps with space grids of 90x45, and 72x30. The significant artificial effect occurs above $n = 45$ ($n = 36$) for synoptic map with grid of 90x45 (72x30). This is understandable.

5.3 The difference between observed coronal holes and predicted footpoints areas obtained using principal index $n = 90, 70, 50, 30$ and spherical harmonic coefficients corresponding to synoptic maps with different space grids is not significant enough to definitely find out which is best fitting observation. We will further investigate it using the HMI synchronic frame (Zhao, Hoeksema and Scherrer, 2009) that is a better proxy of the instatanious global distribution of the line-of-sight photospheric magnetic field than the HMI Carrington synoptic map.

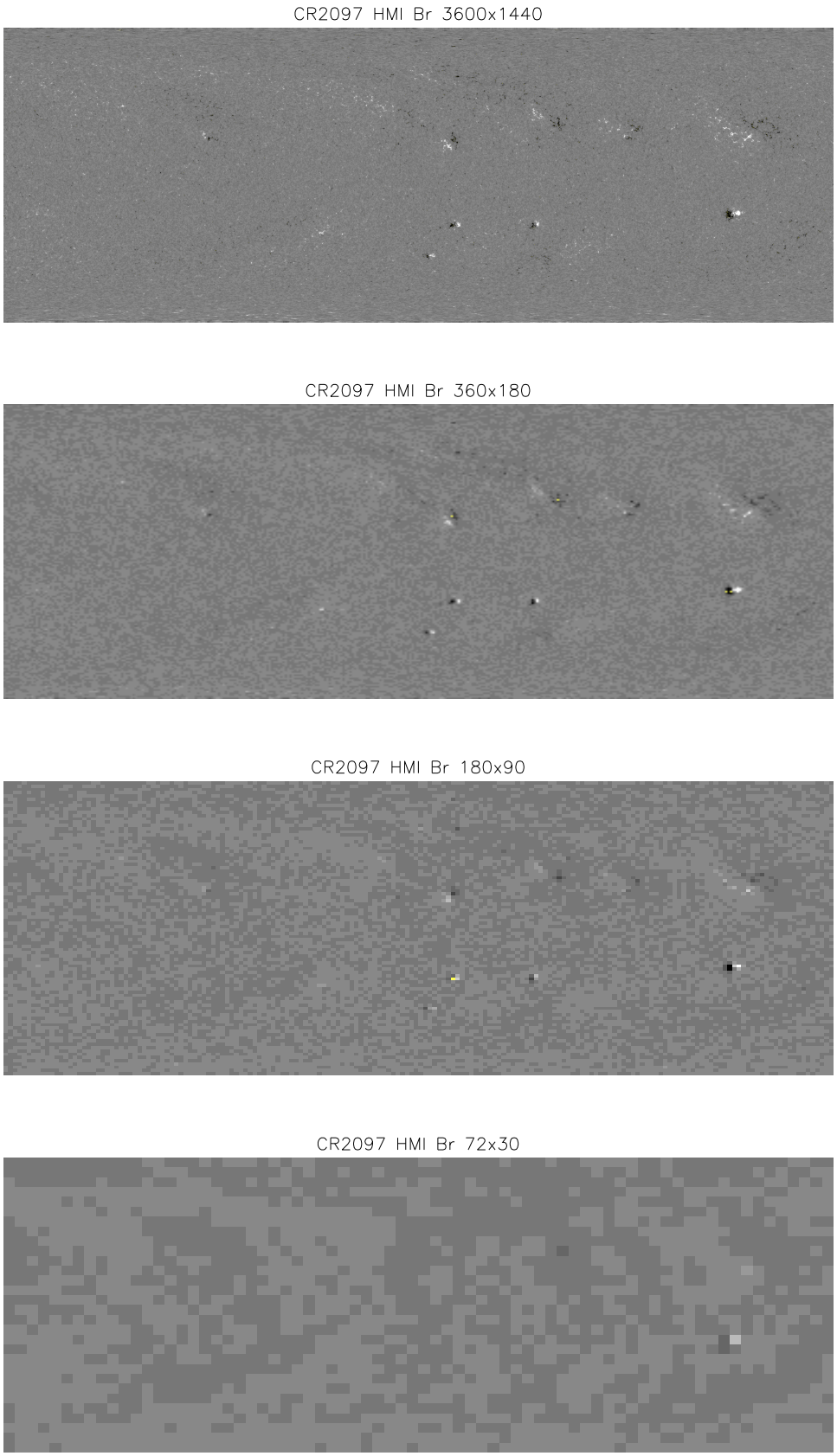

Figure 1. HMI 2097 Carrinton synoptic maps with different synoptic grids, showing magnetic features with different spatial scales.

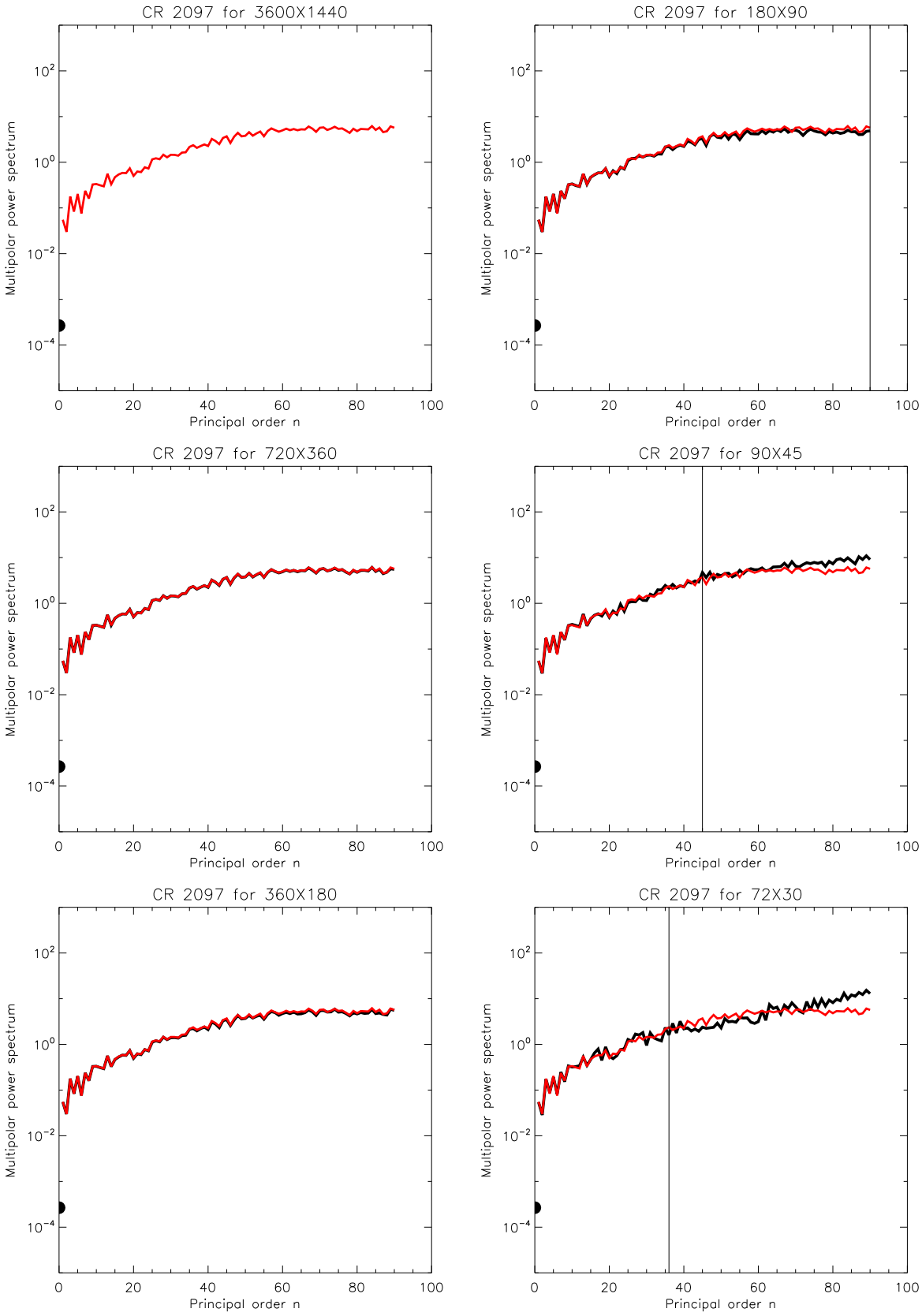

Figure 2. Comparison of multipolar power spectrums obtained from HMI 2097 Carrinton synoptic maps with different synoptic grids. Red curves in all panels denote the power spectrum obtained from HMI synoptic maps of 3600x1440, and black curves from other maps.

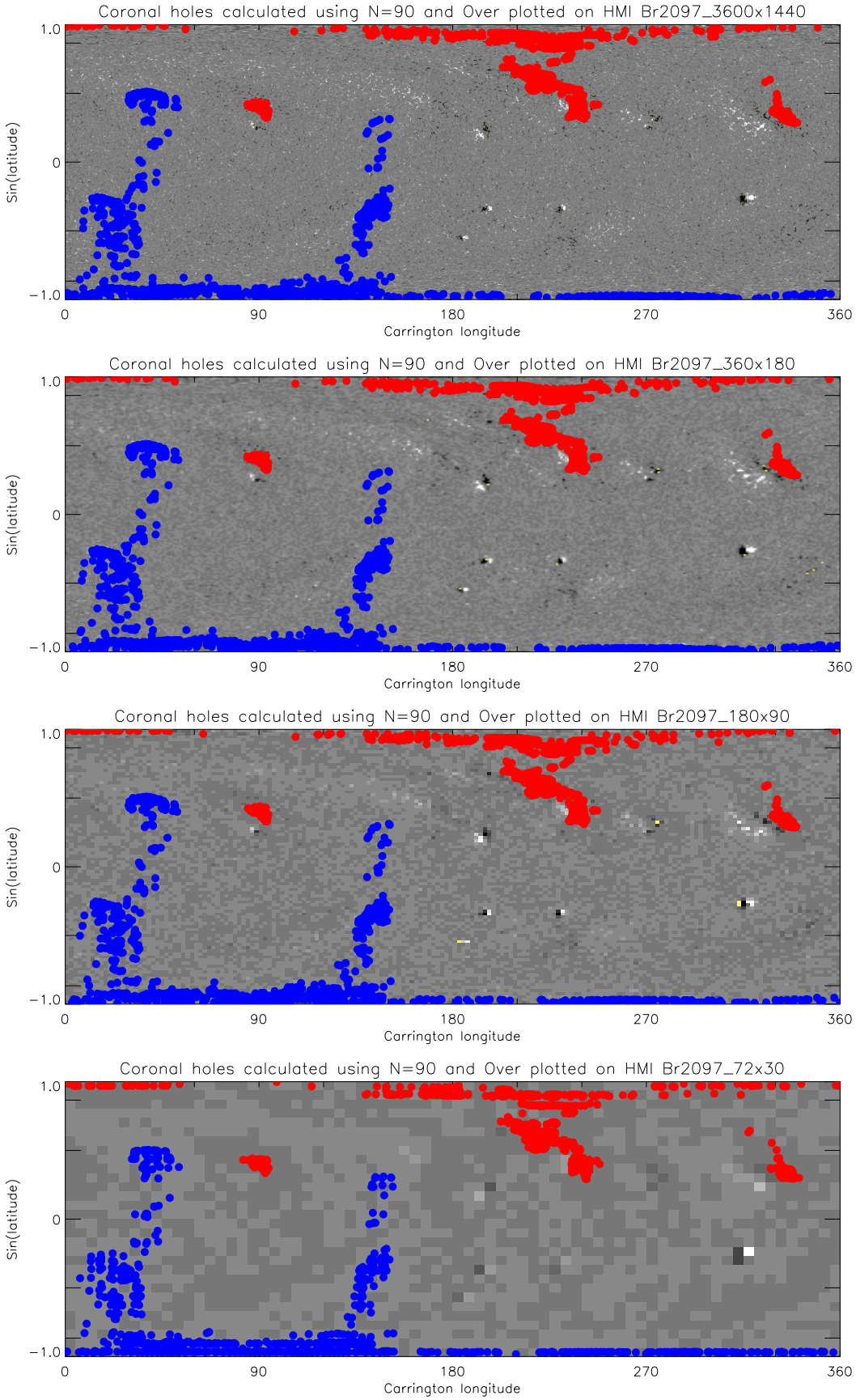

Figure 3a. The open-field foot-points calculated using spherical harmonic coefficients obtained from maps with grids of 3600x1440, 360x180, 180x90, and 72x30 and principal index $n = 90$. Blue and red areas denote positive and negative, respectively.

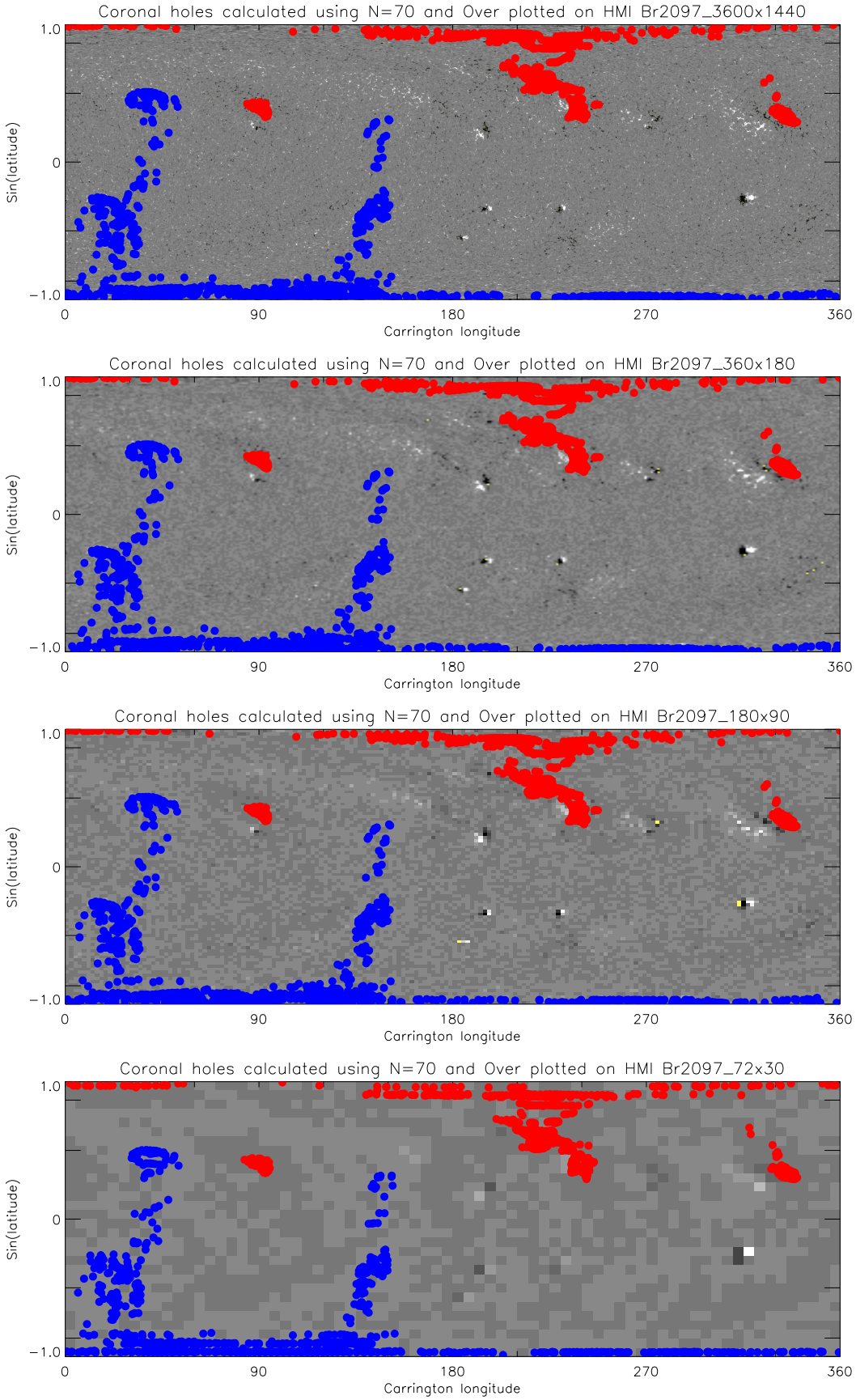

Figure 3b. The same as Figure 3a but $n = 70$.

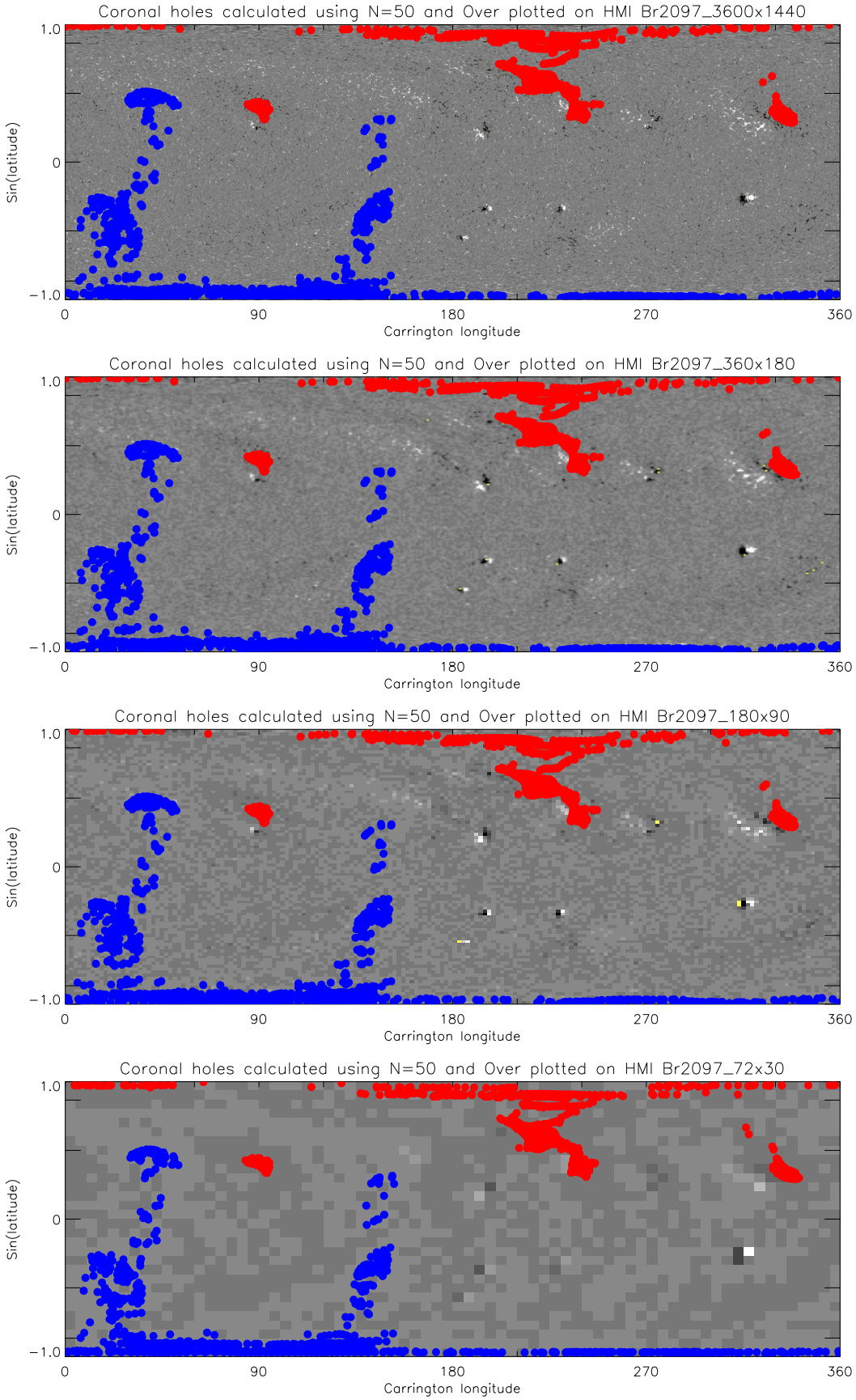

Figure 3c. The same as Figure 3a but $n = 50$.

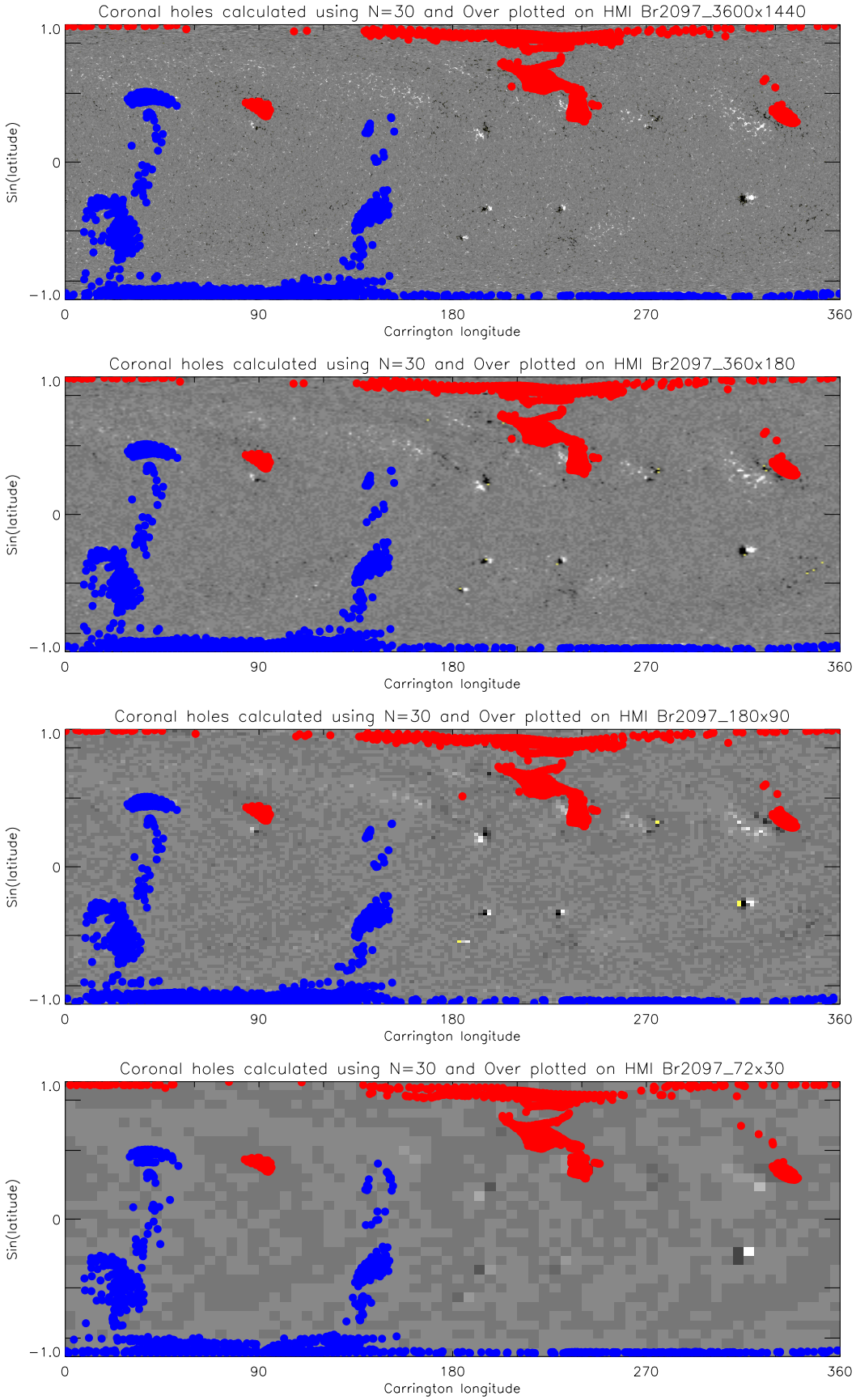

Figure 3d. The same as Figure 3a but $n = 30$.

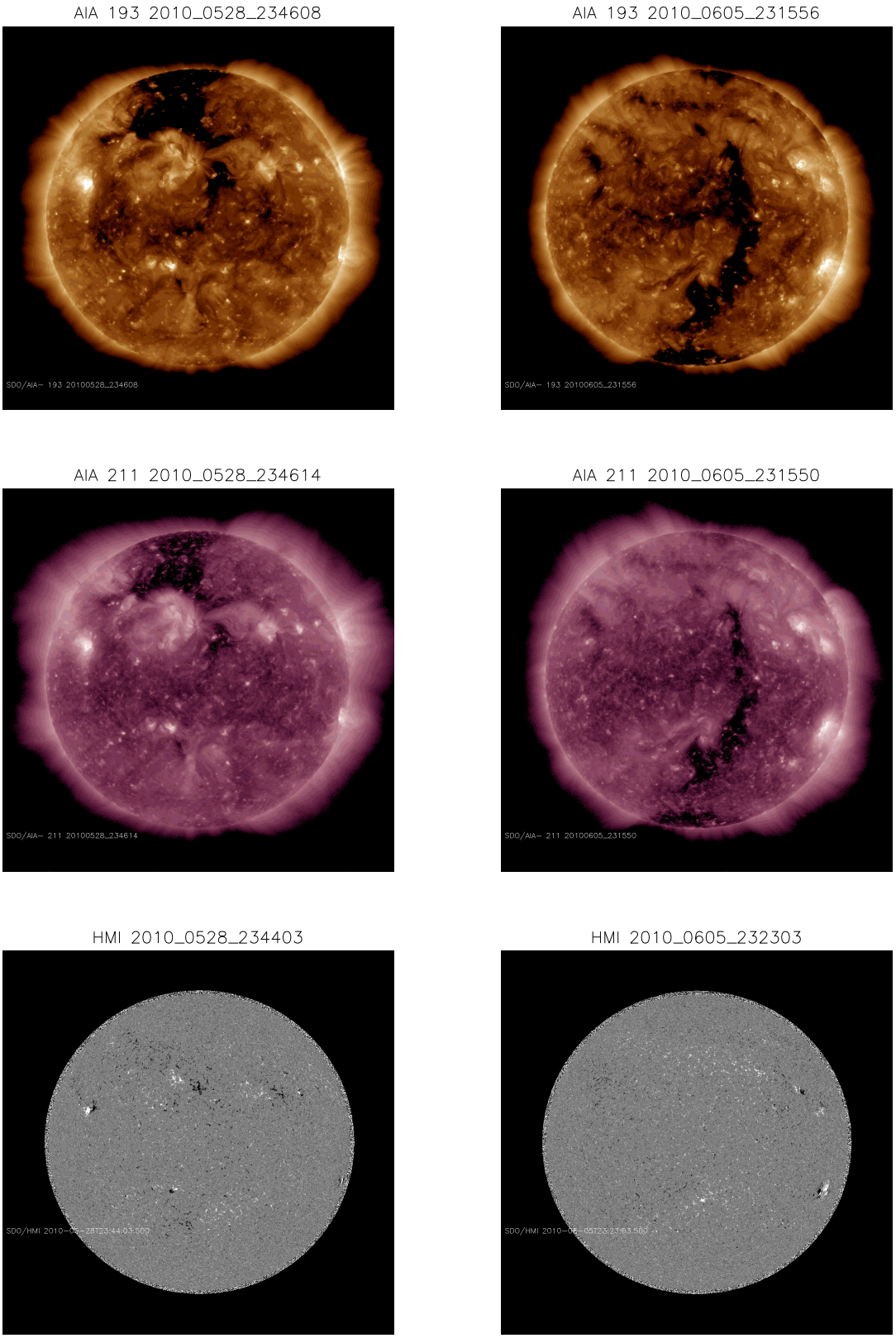

Figure 4. The AIA and HMI images observed around 2010.05.28_23:46:08 and2010.06.05_23:15:56. The dark areas in AIA images are coronal holes.

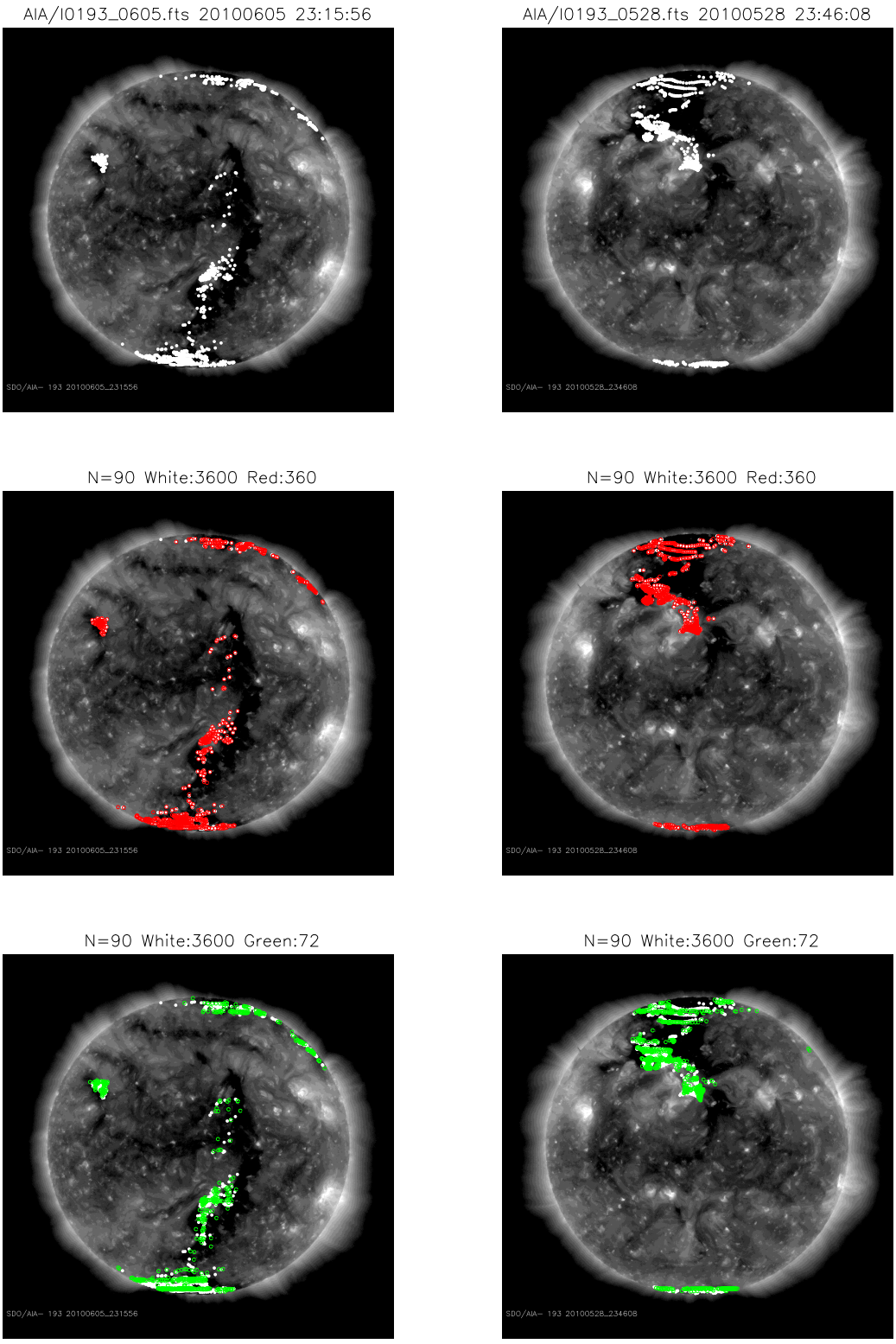

Figure 5a. Comparison of observed coronal holes with foot-points of open field lines calculated using n=90 and spherical harmic coefficients obtained from synoptic maps with grids of 3600x1440 (white), 360x180(red), and 72x30(green), respectively. In the second row the red foot-points are nearly colocated with white points, but in the bottom row, many green points are not colocated with white points.

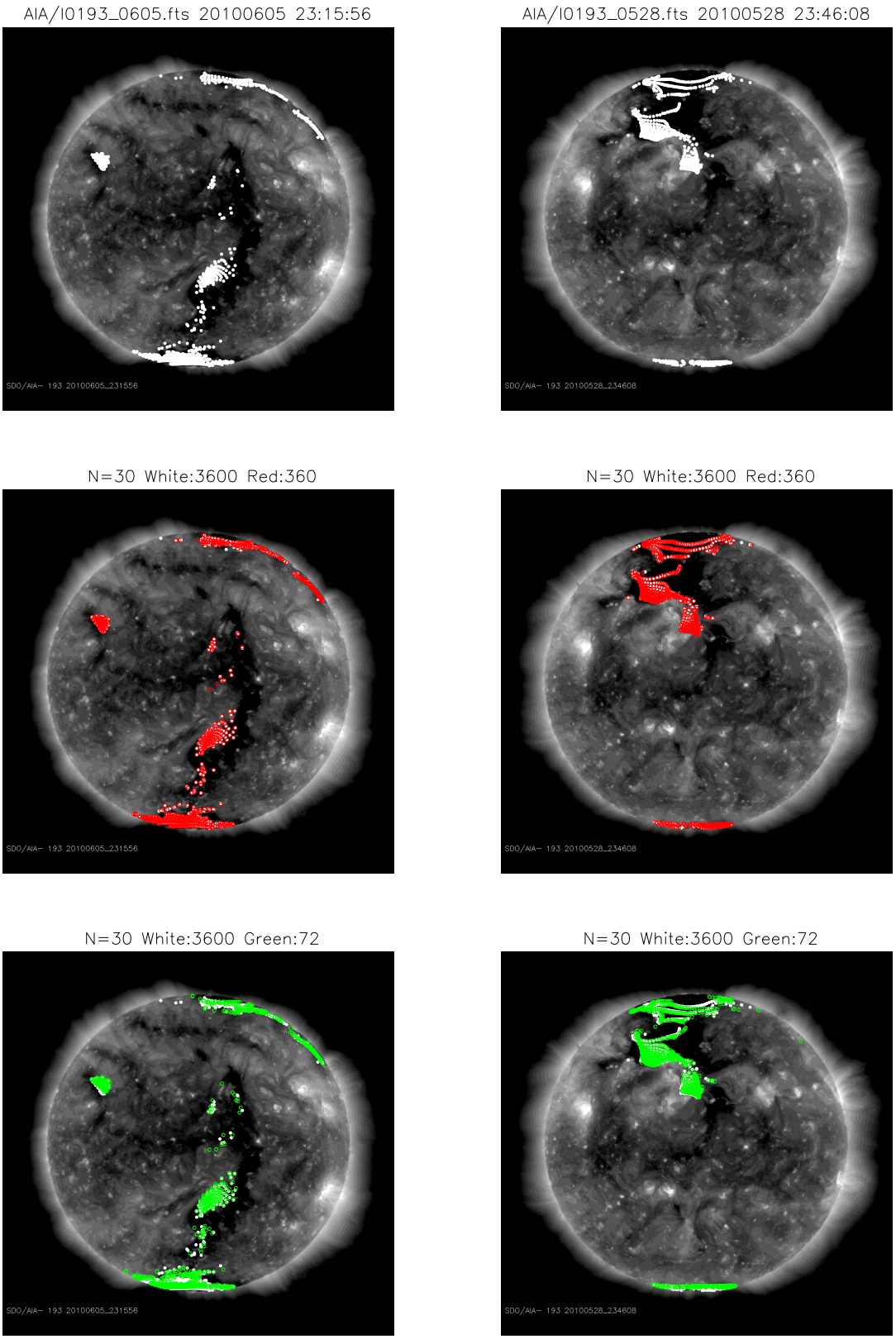

Figure 5b. The same as Figure 5a but $n = 30$.

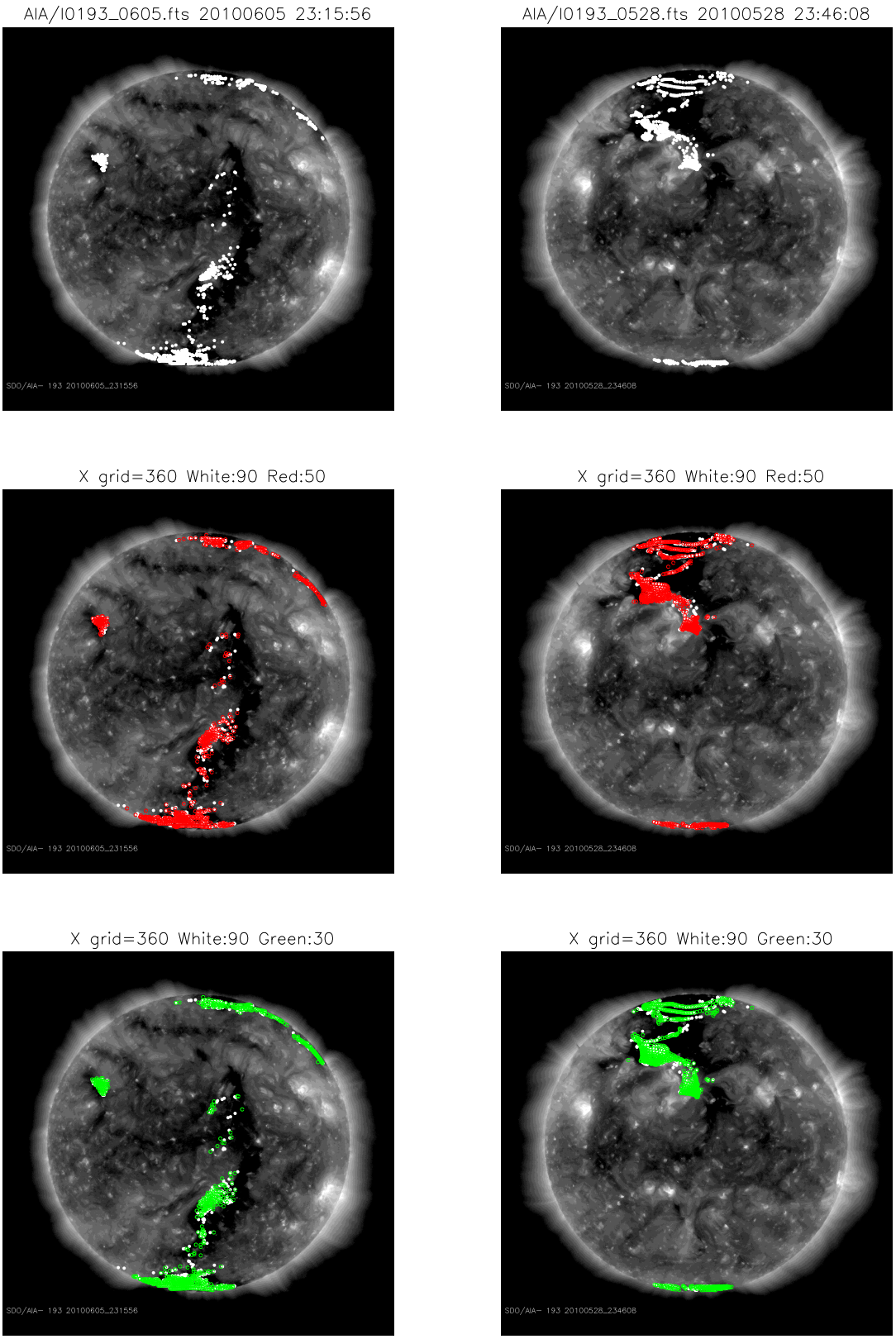

Figure 6a. Comparison of observed coronal holes with foot-points of open field lines predicted using spheric harmonic coefficients from synoptic map of 360x180 and n=90(white), 50(red), 30(green), respectively. Both red and green points are nearly colocated with white points.

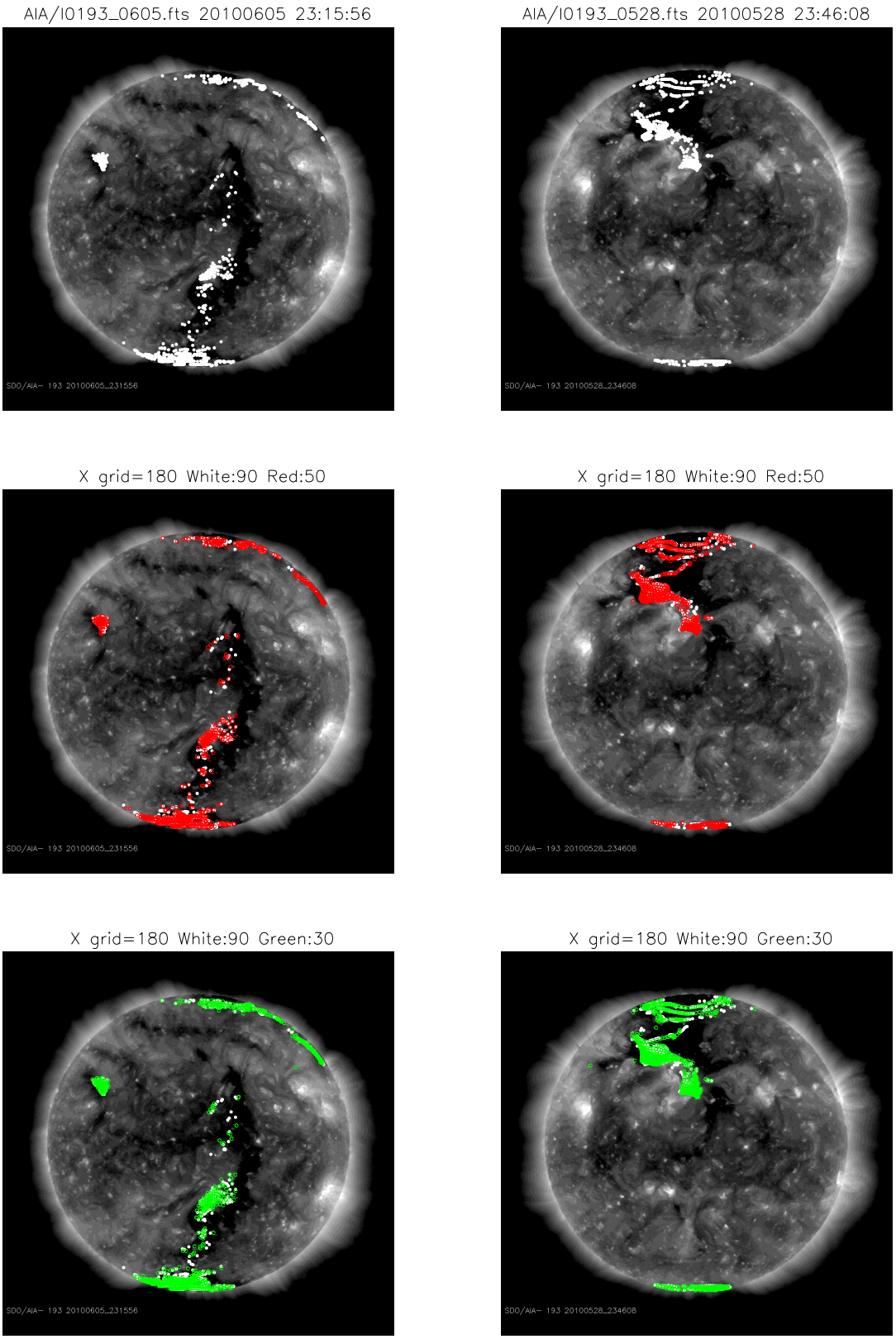

Figure 6b. The same as Figure 6a but using spheric harmonic coefficients from synoptic map of 180x90.

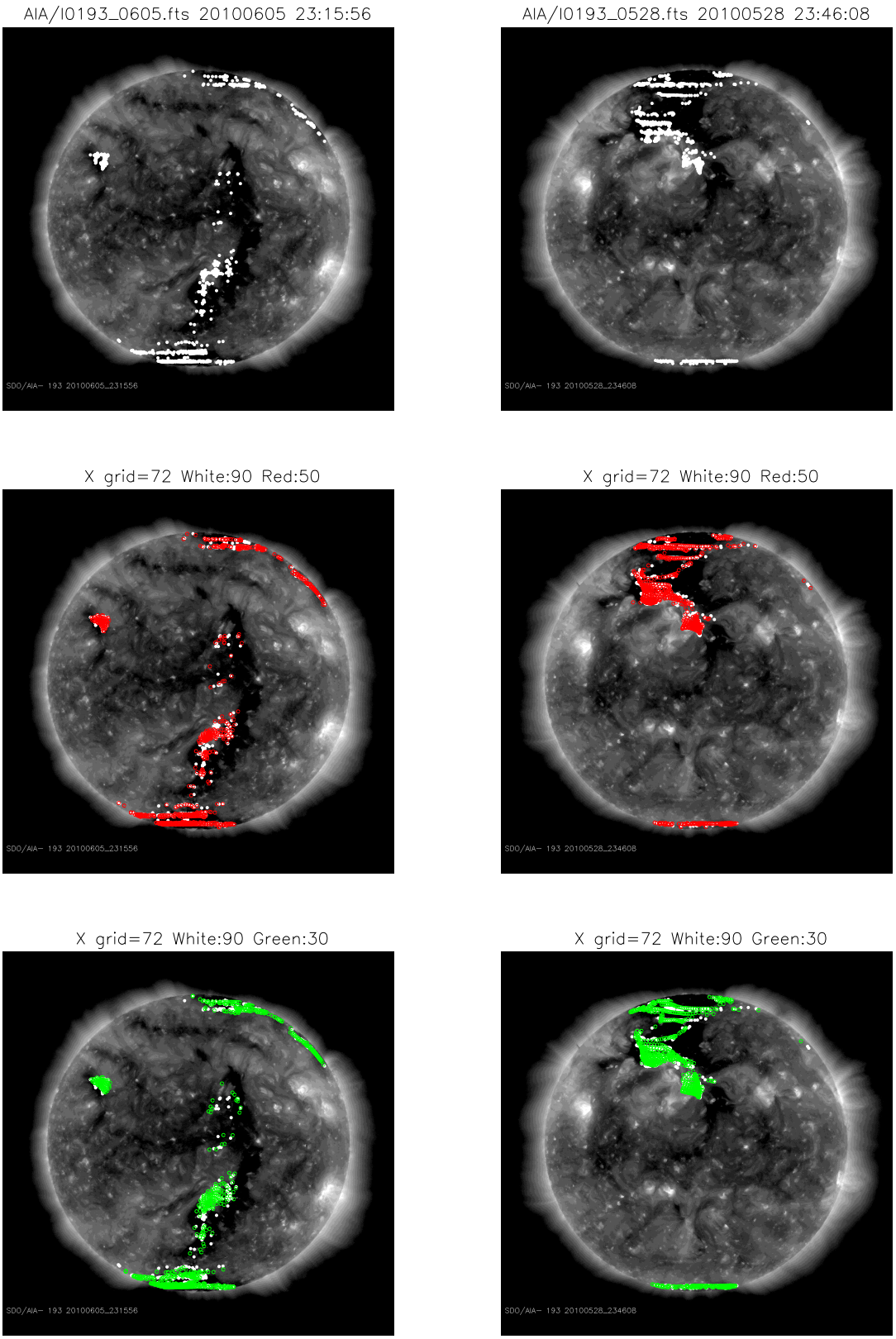

Figure 6c. The same as Figure 6a but using spheric harmonic coefficients from synoptic map of 72x30.